

Optically Transparent Microwave Shielding Hybrid Film Composed by Metal Mesh and Graphene

Xin-Ran Wang^{1, 2, #}, Xiao-Bai Wang^{3, #}, Hang Ren¹, Nan-Shu Wu¹,
Jing-Wen Wu¹, Wen-Ming Su⁴, Yin-Long Han^{3, *}, and Su Xu^{1, 2, *}

Abstract—Transparent conducting materials with the ability of broadband electromagnetic shielding have a widespread range of applications in aerospace, medical equipment, and electronic communications. Achieving enhanced electromagnetic shielding effect without sacrificing much optical transparency is the technical trend in both academia and industries. Here, we experimentally propose a flexible hybrid film constructed by nano-printing based metal meshes and a graphene coating for the transparent electromagnetic shielding application. Numerical analysis is carried out to investigate optimal balance between electromagnetic shielding and optical transparency. In the experiment, enhanced shielding ability of hybrid film is observed without excessively sacrificing optical transmittance, compared to the reference group (the case only with metal mesh). Our work provides a hybrid platform for the high-performance optically transparent shielding materials for electromagnetic environment safety protection.

1. INTRODUCTION

Transparent electromagnetic shielding materials, which prevent electromagnetic radiation from causing harm to personnel or devices at the optically transparent window [1, 2], can find wide industrial applications in the fields of solar energy [3, 4], medical electromagnetic isolation rooms, transparent antennas [5], electronic touch screens, and military utilities [6, 7]. Although the high-performance electromagnetic shielding ability can be achieved through the way of enhancing either reflection or absorption, conventional microwave absorbers and reflective coatings are opaque at visible frequencies due to the material properties of metals and lossy mixtures. As a result, such optically opaque electromagnetic shielding materials cannot be used for the visual observation windows and equipment screens.

To achieve transparent electromagnetic shielding functionalities, optically transparent conductive films, such as carbon nanotubes and Indium Tin oxide (ITO), have been widely studied in both academia and industries [8, 9]. By properly designing and etching the periodic meta-atoms of optically transparent thin film, significant electromagnetic absorption can be achieved at the cost of little optical transmissive insertion loss over a relatively broad frequency spectrum [10]. Different from the absorption-type [11] transparent electromagnetic shielding materials, homogeneous transparent conductive thin films without periodic patterns can achieve reflection-type electromagnetic shielding functionality [12]. Enhanced microwave absorption is also observed in a random disperse system containing conductive (charged) particles [13, 14]. Generally, the reflection-type transparent electromagnetic shielding materials can

Received 21 May 2021, Accepted 1 June 2021, Scheduled 3 June 2021

* Corresponding authors: Yin-Long Han (dragonhan@yeah.net), Su Xu (xusu@jlu.edu.cn). # Xin-Ran Wang and Xiao-Bai Wang are the co-first authors.

¹ State Key Laboratory of Integrated Optoelectronics, College of Electronic Science and Engineering, Jilin University, Changchun 130012, China. ² Zhejiang Provincial Key Laboratory of Advanced Microelectronic Intelligent Systems and Applications, Hangzhou 310027, China. ³ Department of Materials Application Research, AVIC Manufacturing Technology Institute, Beijing 100024, China. ⁴ Printable Electronics Research Centre, Suzhou Institute of Nano-tech and Nano-bionics, Chinese Academy of Sciences, Suzhou 215123, China.

work over a broader bandwidth than the absorption-type ones. This is because homogeneous transparent conductive films are not sensitive to the wavelengths of microwaves as long as the dimension of their basic particle is far smaller than the wavelength of interest [15, 16]. To balance the requirement on optical transparency (i.e., relatively low optical conductivity) and microwave shielding, the thickness of semiconducting transparent films is usually limited within the nanometer scale. Under this limitation, the sheet resistance of homogeneous transparent conductive films is usually higher than $1 \Omega/\square$ [17], which may not meet the electromagnetic shielding requirement for extreme environment (e.g., the high-power electromagnetic pulse over ultrawide frequency spectra).

As the shielding effectiveness of the reflection-type transparent electromagnetic shielding materials is highly related to their own sheet resistance, plasmonics transparent conductive films, such as metal meshes [18–20] and metal nanowire network [21–24], have attracted wide attention for shielding applications. Transparent metal meshes are composed of patterned metallic grid on the surface of transparent dielectric substrate. Generally, the period of the metal mesh is usually much less than the microwave wavelength to achieve strong electromagnetic shielding at microwaves, and at the same time, the period should be much larger than visible-infrared wavelengths to ensure high transmittance at visible region. These characteristics make the metal mesh a good candidate for transparent electromagnetic shielding applications [25, 26]. In 2017, Wang et al. successfully reported a double-layer metal mesh based on a multi-periodic annular nesting structure, which can achieve 90% of the optical transmittance and the 37 dB of maximum electromagnetic SE [27]. With a fixed periodicity and linewidth, the metal mesh can perform a lower sheet resistance and exhibit better shielding performance if the height of metal mesh is increased. However, the metal mesh with increased height, on one hand, is not easy to fabricate on the large area of substrate, and on the other hand, it may make the optical observation window hazed. For this reason, two-dimensional conducting materials, e.g., graphene, have shown great potential in high-performance transparent electromagnetic shielding due to nanometer-scale thickness [28–35]. Recently, it is reported that hybrid films of graphene and micro-structured metals can effectively improve the conductivity of the structure while maintaining excellent optical transmittance [36, 37]. Since the performance of microwave shielding is highly related to the conductivity of the material, the graphene coated metal mesh may exhibit great electromagnetic shielding [38].

In this paper, we study the microwave shielding effectiveness (SE) and optical transmittance of the hybrid structure constructed by metal meshes and graphene (Fig. 1). The relationship among microwave SE, optical transmittance at visible regime, and the structural property of metal meshes is analyzed. On the basis of aforementioned analysis, the metal mesh-graphene hybrid structure is fabricated through nanoimprinting and chemical vapor deposition (CVD). The experimental results show that the hybrid structure can achieve 31.8 dB average SE over the frequency range from 9.5 to 11.5 GHz with the average optical transmittance of 77.3% from 400 nm to 780 nm. Our work indicates that the graphene-metal mesh hybrid structure can be applied to transparent electromagnetic shielding scenarios with strict performance demand.

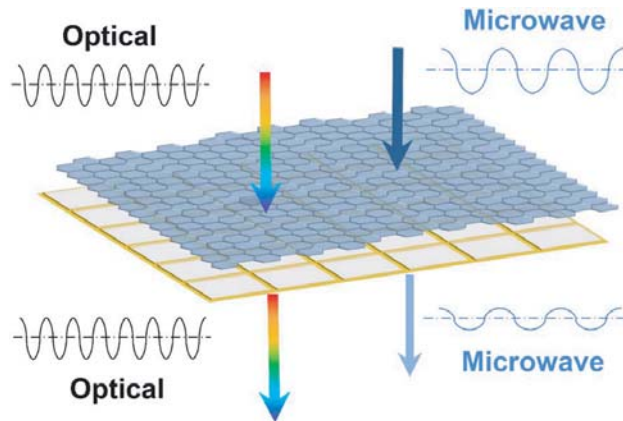


Figure 1. Schematic view of the hybrid structure of metal mesh and graphene for transparent electromagnetic shielding applications.

2. DESIGN AND SIMULATION

We start the SE analysis from various structural properties of metal meshes. CST Studio Suite is selected for simulation and design. In the simulation, we only consider a single unit-cell of the metal mesh whose dimensions are given in Fig. 2(a), and the number of total meshes in the simulation is

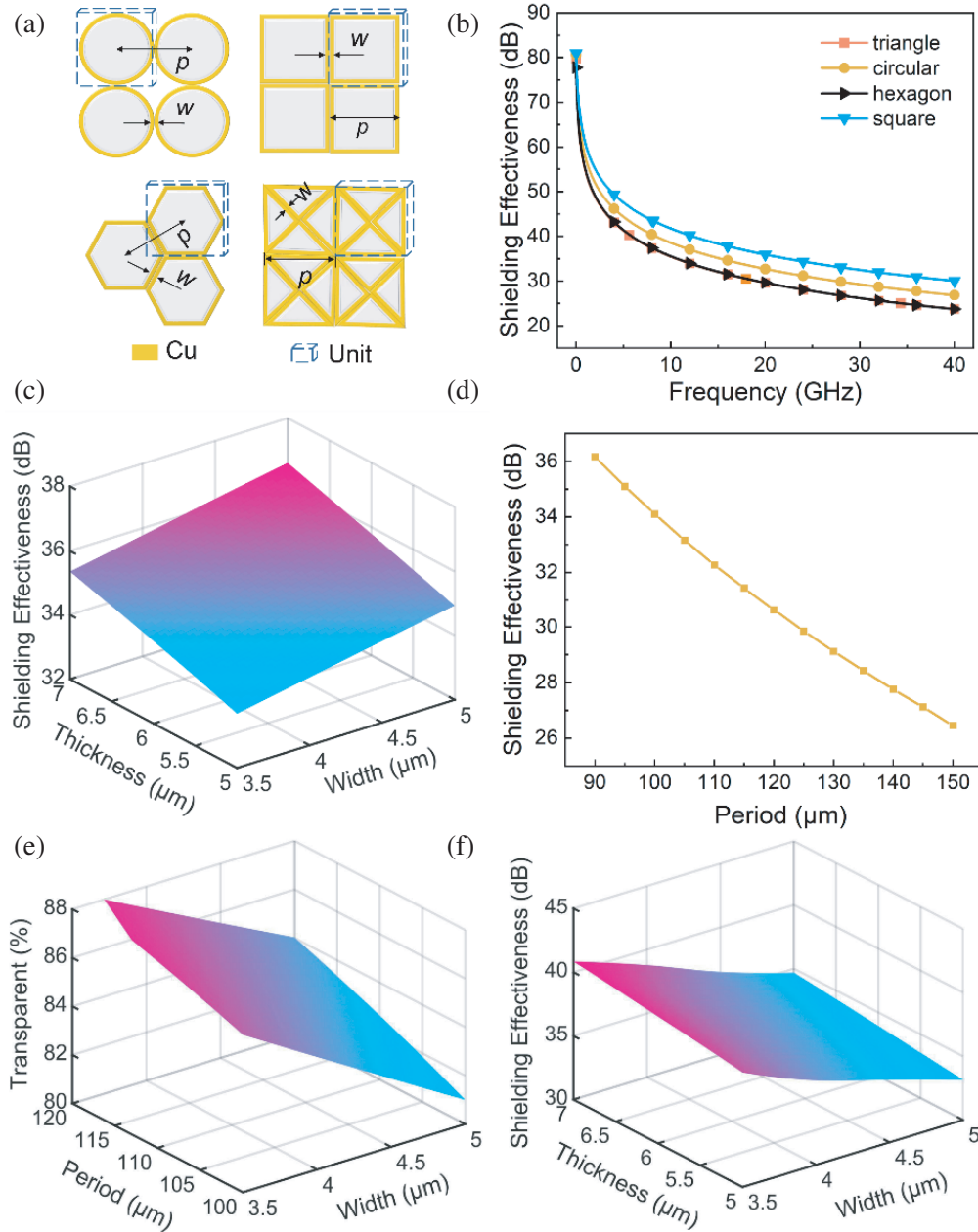


Figure 2. Numerical shielding effectiveness and optical transmittance of various metal meshes. (a) The geometrical properties of metal-mesh unit cells. (b) The SE comparison among four kinds of the metal mesh with the optical transmittance of 85%. (c) The SE of square-lattice metal mesh with the various thicknesses and linewidths. (d) The SE of square-lattice metal mesh with the various periods. (e) The transparency of square-lattice metal mesh with different periods and widths. (f) The SE trend with various thicknesses and widths when the optical transmittance is fixed at $T_{opt} = 85\%$ for the case of square-lattice metal mesh. The numerical analysis of metal mesh in Figs. 2(c)–(f) is focused at 40 GHz. Here, we focus on the metal mesh and neglect the influence of substrate.

about $10^3 \sim 10^4$ for different cases. In the simulation, the background is air; the boundaries are unit-cell boundaries; and the metal used is copper with the electric conductivity of 5.96×10^7 S/m. Totally four kinds of periodic structure, i.e., square, circular, hexagonal, and triangle lattices, are used for studying the geometrical influence on the SE, as shown in Fig. 2(a). Since the periodicities of metal meshes are usually far smaller than the wavelength of interest at microwave regime, effective medium theory (EMT) can be used for theoretically deriving the low-frequency electric conductivity or sheet resistance of the metal meshes [39, 40]. The sheet resistance of a homogeneous film can be derived as $R_s = \rho/t$, where ρ and t are the resistivity and thickness of the conductive film, respectively. Moreover, $\rho = R \cdot S/L$, where R is the value of resistance; L and S are the length and area of the material. The sheet resistance for a nanopatterned conductive film is calculated by $R_s = (\frac{\rho}{t}) \cdot (\frac{p}{w})$, which depends on the two-dimensional period p and metal width w as well [41]. Therefore, the filling factor of the metal is the key factor affecting R_s . Different from the EMT model for low-frequency electric conductivity, the optical transmittance or optical conductivity at normal incidence can be easily calculated from the filling factor of metals, which was discussed [42]. Since the linewidth of the metal mesh is much larger than the wavelength of visible light, the metal can be regarded as causing total reflection, and the rest of the metal mesh can be treated as total transmission under the normal incidence. With such assumption, the transmittance (T_{opt}) is expressed as $T_{opt} = S_{metal}/S_{whole} \times 100\%$. For the case of the square-lattice metal mesh, the transmittance can be written by $T_{opt} = (p - w)^2/p^2 \times 100\%$. Based on these two different calculation models, the electromagnetic SEs for the cases of the aforementioned four kinds of metal mesh are simulated numerically over the frequency band from 0 to 40 GHz under different conditions. In the numerical analysis, we focus on the metal mesh and neglect the influence of substrate.

Firstly, the transmittance T_{opt} of four kinds of metal meshes are set at the same value, e.g., $T_{opt} = 85\%$ to evaluate the impact of distinct shapes on the metal mesh film. Under this condition, the geometrical properties of metal meshes are: $p = 99.46 \mu\text{m}$, $w = 3.88 \mu\text{m}$ for the case of circular lattice; $p = 64 \mu\text{m}$, $w = 5 \mu\text{m}$ for the case of square lattice; $p = 96 \mu\text{m}$, $w = 7.49 \mu\text{m}$ for the case of hexagonal lattice; $p = 154.7 \mu\text{m}$, $w = 6.07 \mu\text{m}$ for the case of triangular lattice. The thicknesses of metal mesh for all the cases are set at $t = 5 \mu\text{m}$. Through the numerical simulation, the corresponding SEs are shown in Fig. 2(b). One can see that the metal mesh with a square unit cell can achieve a higher SE than the other three cases. Additionally, through Fig. 2(b), one can also see that the electromagnetic SE of the structural metal mesh decreases when the frequency increases, which can be explained by the effective medium theory.

Secondly, the SE of square-lattice metal mesh with various thicknesses and linewidths is studied in Fig. 2(c). Here, the period is fixed at $100 \mu\text{m}$, while the thickness and linewidth of metallic wire vary from $5 \mu\text{m}$ to $7 \mu\text{m}$ and from $3 \mu\text{m}$ to $5 \mu\text{m}$, respectively. One can see that the electromagnetic SE of the square-lattice metal mesh is improved when both the thickness and linewidth are increased. Similarly, the relationship between the period and electromagnetic SE of the square-lattice metal mesh is shown in Fig. 2(d). The linewidth and thickness are fixed at $3.5 \mu\text{m}$ and $7 \mu\text{m}$. The simulation result illustrates that the electromagnetic SE of the metal mesh decreases when the period increases. Therefore, the increased linewidth (thickness), or the decreased period, will make the overall sheet resistance of the metal mesh decline, which leads to the enhancement of the electromagnetic SE.

Thirdly, the optical transmittance of the metal mesh depends on its period and linewidth, whose results are shown in Fig. 2(e). The period and linewidth of the square-lattice metal mesh vary from $100 \mu\text{m}$ to $120 \mu\text{m}$ and from $3.5 \mu\text{m}$ to $5 \mu\text{m}$, respectively. The result shows that the optical transmittance of the square-lattice metal mesh increases when the metallic line decreases in width, or the period of the metal mesh increases.

In accordance with the analysis above, the optical transmittance and electromagnetic SE are mutually restricted when the linewidth and period of the metal mesh are changed. With a fixed optical transmittance ($T_{opt} = 85\%$), the relationship between electromagnetic SE and the linewidth and period of squared lattice is shown in Fig. 2(f), which is helpful to select appropriate parameters for achieving the required electromagnetic SE and optical transmittance of the metal mesh. The practical realization of industrial shielding material constructed by metal mesh and graphene can benefit from the previous discussion on the geometries of metal meshes.

3. MATERIALS AND METHODS

After optimizing and selecting the proper geometrical property of metal mesh, the remaining issue is to achieve the metal mesh and further transfer the graphene onto the metal mesh in practice. The whole fabrication and material preparation procedure is schematically shown in Fig. 3.

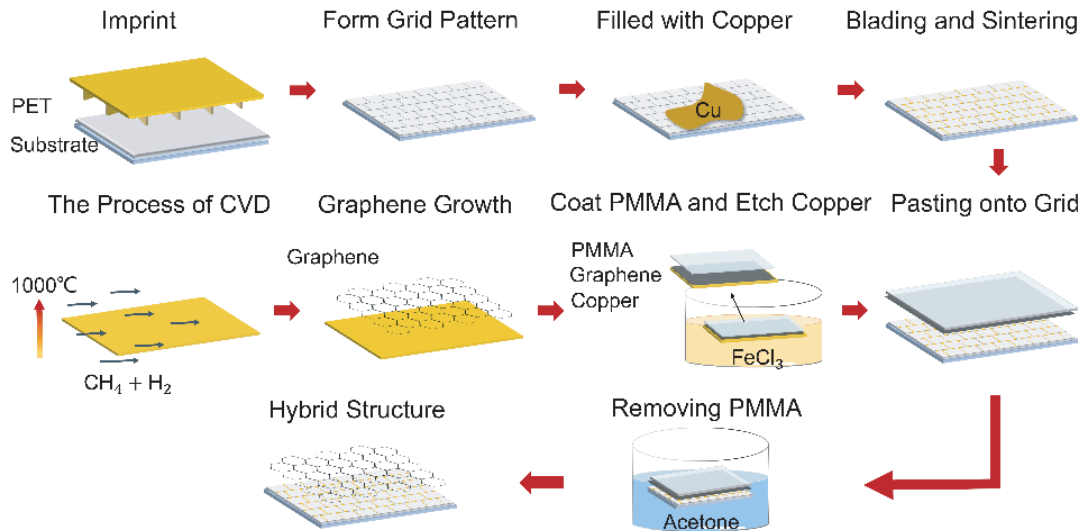


Figure 3. Synthesis process for the metal mesh-graphene hybrid film.

3.1. Fabrication of the Metal Mesh Film

The metal mesh is fabricated through nanoimprinting technique [43]. Firstly, the photoresist is spin-coated on the cleaned and dried glass substrate and gets the groove mesh pattern by exposure and development. Then silver mirror reaction is performed on the mask, and it is placed in the electroplating device for nickel plating and finally forms an imprinted nickel plate. After the nickel plate is prepared, the groove structure is imprinted on a PET substrate whose relative permittivity is about $\epsilon_r = 3 * (1 - j0.006)$ [44] with the thickness of 0.175 mm and dimension of 25 mm * 15 mm. This process will be divided into three steps: (1) the photoresist is covered on the PET substrate; (2) the nickel plate is imprinted on the PET substrate and cured by an ultraviolet lamp; (3) grooves are filled with copper nanoparticles and solidified using flash sintering.

3.2. Graphene Synthesis

The graphene is fabricated through CVD [45]. First of all, the processed copper foil is placed at the center of the test tube furnace, and the foil is heated to 1000° for 30 minutes with protective gas passing. Secondly, the carbon source gas, CH_4 , is passed through the tube furnace for 1 hour to react after the temperature is stable. Then, the graphene-coated copper foils can be obtained when the tube is cooled to room temperature.

3.3. Graphene Transferring and Hybrid Film Assembling

The graphene is transferred to the metal mesh film by wet chemical etching substrate. Firstly, the transfer medium, PMMA is spin-coated on the surface of the graphene for 1 min at 3500 rpm as a support layer. Then, PMMA-graphene covered copper foil is immersed in the FeCl_3 solution to corrode the copper substrate. Next, the PMMA-graphene film is cleaned and transferred to the metal mesh film. At last, the PMMA-graphene-metal mesh film is placed into an acetone bath to remove PMMA. The hybrid films constructed by metal meshes which are encapsulated between the substrate and the graphene are completed.

After all the fabrication procedure, three groups of hybrid samples (i.e., Samples 1 to 3) with different values of graphene's sheet resistance are obtained in addition to a group of pure metal mesh (i.e., the reference group).

4. CHARACTERIZATION AND DISCUSSION

4.1. Spectroscopic Characterization

The surface topography of the square-lattice metal mesh is characterized with the use of scanning electron microscopy (SEM), whose results are shown in Fig. 4(a). One can see that good electrical connection is built after imprinting and sintering. A good electrical connection indicates that the metal mesh can be used for electromagnetic shielding application. To confirm graphene being transferred to the metal mesh, Raman measurement is conducted using the laser with wavelength of 532 nm. As shown in Fig. 4(b), two characteristic peaks of graphene, i.e., the G peak at 1582 cm^{-1} and the 2D peak 2681 cm^{-1} at cm^{-1} , can be observed in the test. The Raman spectra indicate the graphene has been transferred to the metal mesh already. Additionally, the D peak around 1350 cm^{-1} , which is related to the disorder, cannot be observed from the measurement, which typifies that the transferred graphene is defect-free on the metal mesh.

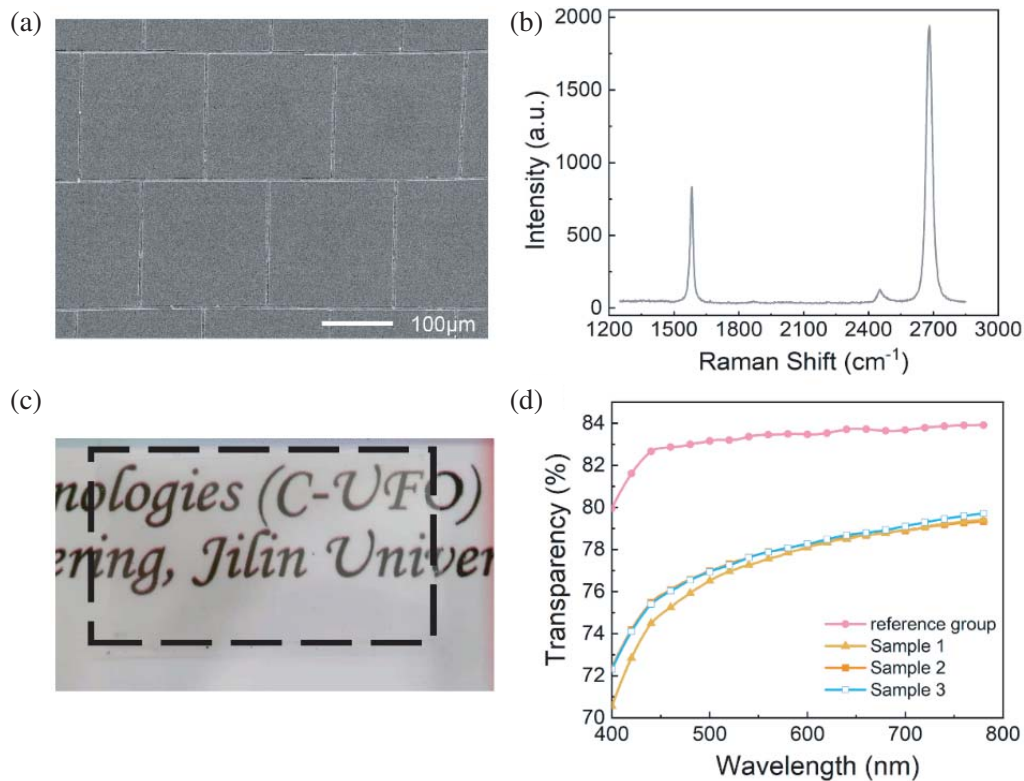


Figure 4. (a) The SEM image of metal mesh. (c) The hybrid film above a picture. (d) The optical transmittance of reference group (metal mesh) and hybrid films with different sheet resistance. Considering the convenience on practical fabrication, the period and linewidth of the square-lattice metal mesh are $170\text{ }\mu\text{m}$ and $4\text{ }\mu\text{m}$ here, respectively.

4.2. Optical Characterization

Figure 4(c) shows the real picture of the hybrid film over the picture with the content of “Jilin University”. Penetrating through the sample, the image and information on the picture can be clearly found. As shown in Fig. 4(d), the optical transmittance for the cases of three hybrid films and one metal

mesh layer is measured as comparison. In the wavelength range from 400 nm to 780 nm, the average optical transmittance of the metal mesh layer and hybrid films (Sample 1, Sample 2, and Sample 3) is above 83.29%, 77.31%, 77.66%, and 77.72%, respectively. Compared with the metal mesh, the samples coated with the graphene reduce their optical transmittance by about 6%.

4.3. Microwave SE Test

In order to verify the electromagnetic SE of the metal mesh-graphene hybrid film, the sheet resistance of three samples and metal mesh is firstly measured by the Four-Point Probes. The sheet resistance of the reference group before integrating with the graphene is $0.43 \Omega/\square$. In contrast, the sheet resistances of Sample 1, Sample 2, and Sample 3 decrease to $0.26 \Omega/\square$, $0.30 \Omega/\square$, and $0.40 \Omega/\square$, respectively. Note that the measured sheet resistance may be slightly different from the practical values because the Four-Point Probes may not touch the hybrid films and metal mesh exactly. The hybrid samples are tested through a Vector Network Analyzer as shown in Fig. 5. Since the dimension of sample is limited by the transferred graphene, the microwave experiment is carried out in a rectangular waveguide (WR-90), whose frequency range of fundamental mode is over 8.2 to 12.4 GHz. To avoid the potential influence of cut-off region and multiple waveguide modes, we only select the frequency range from 9.5 GHz to 11.5 GHz to obtain the results. Although we only measure the SE over a relatively narrow frequency range, we believe that the microwave SE can be achieved over a relatively wide range, as long as the periodicity of metal mesh is far smaller than the wavelength of interest, according to the numerical simulation. Through the test, one can see that the average SEs of Samples 1 to 3 and the reference group are 31.8 dB, 30.9 dB, 30.1 dB, and 26.2 dB, respectively. It is clear that the electromagnetic SE for the case of hybrid structures is enhanced compared to the reference group. Additionally, one can see that the electromagnetic SE is improved by about 5.11 dB for the case of Sample 1, 4.5 dB for the case of Sample 2, and 2.2 dB for the case of Sample 3, compared to the reference group at the center frequency of the testing band, i.e., 10.5 GHz, while the average optical transmittance only decreases by 6%. Although the simulated curve is relative flat and standing waves occur in the experiment, the SE curves of metal mesh and hybrid film still show a similar trend to the simulated one. The difference on the magnitude of SE and spectral SE changing rate may be related to the imperfection during the fabrication (e.g., blading nanoink amount and sintering homogeneity) and measurement (e.g., mechanical cutting edge of periodic structure, to match the dimension of straight waveguide).

The transfer process of the electromagnetic wave can be used to describe and explain shielding

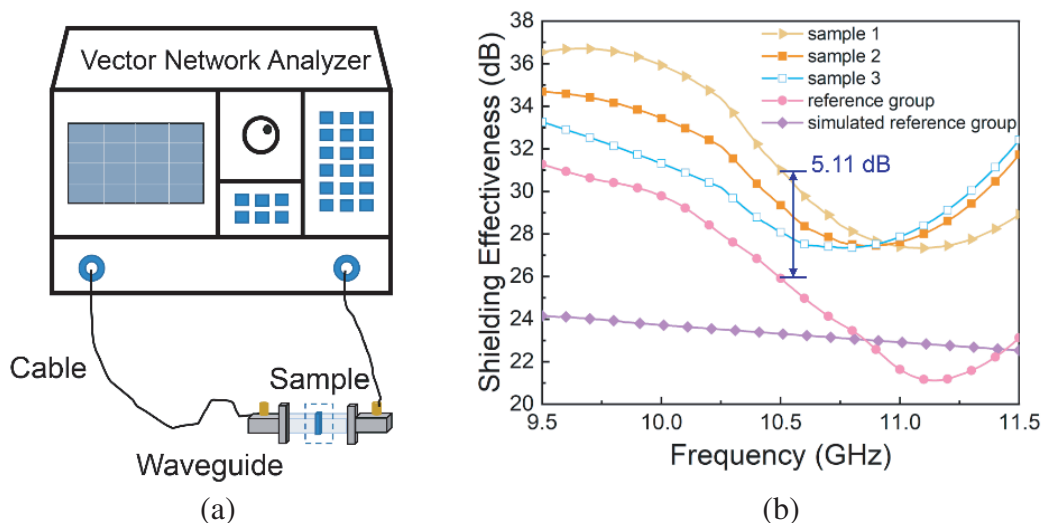


Figure 5. (a) The schematic diagram of the waveguide testing system. (b) The electromagnetic SE of reference group (pure metal mesh), Samples 1, 2, and 3. Limited by the test environment, the SE performance is measured over the frequencies from 9.5 to 11.5 GHz.

mechanism [46]. When the incident waves are exposed to the hybrid film, part of electromagnetic waves are reflected because of the impedance mismatch caused by the difference between the conductivities of air and the material. The huger difference will result in more reflection. In addition, the penetrating electromagnetic waves have multiple reflection and absorption between the metal mesh layer and graphene layer, which contributes to the energy loss of electromagnetic waves. The experimental results that we obtained show the same trend.

The performances of previous state of art [47–51] are compared to our work in Fig. 6. One can see that our hybrid film can not only achieve outstanding microwave SE but also have relatively high optical transparency. For practical applications, our work can improve the SE compared to the pure metal mesh with the help of graphene, which may meet the higher requirements of transparent and flexible electromagnetic shielding in industrial or military fields. On the other hand, graphene will bring additional continuous conducting effects for higher frequency, as the geometrical property of fundamental “meta-atom” of graphene is far smaller than the wavelength of microwaves and even millimeter waves. This continuous surface effects will extend the SE bandwidth of single metal mesh that is limited by the effective medium theory, from microwave to higher frequencies.

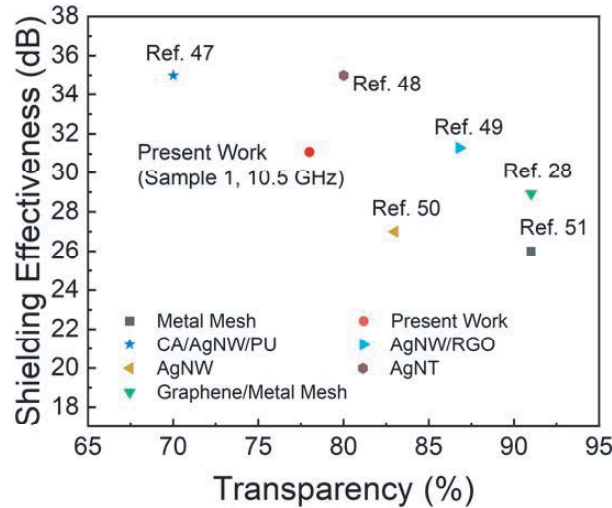


Figure 6. SE and visible transmittance for different transparent electromagnetic shielding materials.

5. CONCLUSION

In this paper, we design and study the SE of the flexible hybrid films constructed by nano-printing based metal meshes and a graphene coating in both numerical simulation and experiments. Numerical analysis is carried out to investigate optimal balance between electromagnetic shielding and optical transparency. Intuitively, higher SE is provided with lower transmittance. The optimization between the transmittance and SE can be gained by properly controlling the width and period of the metal mesh. In the experiment, an enhanced SE of hybrid film is observed without excessively sacrificing optical transmittance compared to the case only with metal mesh. Compared with the metal mesh, the electromagnetic SE of hybrid samples can be increased by 5.11 dB (Sample 1) at the center frequency of the testing band, i.e., 10.5 GHz, as shown in Fig. 5(b), only by sacrificing 5.89% (Sample 1) average optical transparency. As the graphene can amend the material homogeneity of the structural shielding film, e.g., metal mesh at higher frequencies, the hybrid shielding film constructed by graphene and metal mesh may work at not only microwaves but also higher frequencies, such as millimeter waves. Our work provides a hybrid platform for the high-performance optically transparent shielding materials for electromagnetic environment safety protection over ultra-wide frequency spectra.

ACKNOWLEDGMENT

This work was sponsored by the National Natural Science Foundation of China (NSFC) Grant Nos. 61805097 and 61935015. S. X. acknowledges the Support from the open project of Zhejiang Provincial Key Laboratory of Advanced Microelectronic Intelligent Systems and Applications.

REFERENCES

1. Weng, G. M., et al., "Layer-by-layer assembly of cross-functional semi-transparent MXene-Carbon nanotubes composite films for next-generation electromagnetic interference shielding," *Advanced Functional Materials*, Vol. 28, 1803360, 2018.
2. Liu, J., et al., "Hydrophobic, flexible, and lightweight MXene foams for high-performance electromagnetic-interference shielding," *Advanced Materials*, Vol. 29, 1702367, 2017.
3. Liu, Y. S., et al., "Ultrasoother, highly conductive and transparent PEDOT: PSS/silver nanowire composite electrode for flexible organic light-emitting devices," *Organic Electronics*, Vol. 31, 247, 2016.
4. Bi, Y. G., et al., "Broadband light extraction from white organic light-emitting devices by employing corrugated metallic electrodes with dual periodicity," *Advanced Materials*, Vol. 25, 6969, 2013.
5. Hu, H. T., et al., "A transparent proximity-coupled-fed patch antenna with enhanced bandwidth and filtering response," *IEEE Access*, Vol. 9, 32774–32780, 2021.
6. Cho, S., et al., "Large-area cross-aligned silver nanowire electrodes for flexible, transparent, and force-sensitive mechanochromic touch screens," *ACS Nano*, Vol. 11, 4347–4357, 2017.
7. Lin, S., et al., "Roll-to-roll production of transparent silver-nanofiber-network electrodes for flexible electrochromic smart windows," *Advanced Materials*, Vol. 29, 1703238, 2017.
8. Shen, Y., et al., "Transparent broadband metamaterial absorber enhanced by water-substrate incorporation," *Optics Express*, Vol. 26, 15665–15674, 2018.
9. Wu, Z. C., et al., "Transparent conductive carbon nanotube films," *Science*, Vol. 305, 1273–1276, 2004.
10. Zhang, C., et al., "Broadband metamaterial for optical transparency and microwave absorption," *Applied Physics Letters*, Vol. 110, 143511, 2017.
11. Lv, T. T., et al., "Switchable dual-band to broadband terahertz metamaterials absorber incorporating a VO₂ phase transition," *Optics Express*, Vol. 29, 5437–5447, 2021.
12. Wang, H., et al., "Double-layer interlaced nested multi-ring array metallic mesh for high-performance transparent electromagnetic interference shielding," *Optics Letters*, Vol. 42, 1620, 2017.
13. Kocifaj, M., et al., "Charge-induced electromagnetic resonances in nanoparticles," *Annalen der Physik*, Vol. 527, 765–769, 2015.
14. Klacka, J., et al., "Optical signatures of electrically charged particles: Fundamental problems and solutions," *Journal of Quantitative Spectroscopy & Radiative Transfer*, Vol. 164, 45–53, 2015.
15. Dang, M. T., et al., "Recycling Indium Tin Oxide (ITO) electrodes used in thin-film devices with adjacent hole-transport layers of metal oxides," *ACS Sustainable Chemistry & Engineering*, Vol. 3, 3373–3381, 2015.
16. Cairns, D. R., et al., "Strain-dependent electrical resistance of tin-doped indium oxide on polymer substrates," *Applied Physics Letter*, Vol. 76, 1425–1427, 2000.
17. Zhang, Y. K., et al., "Solution-processed transparent electrodes for emerging thin-film solar cells," *Chemical Reviews*, Vol. 120, 2049–2122, 2020.
18. Han, Y., et al., "Crackle template based metallic mesh with highly homogeneous light transmission for high-performance transparent EMI shielding," *Scientific Reports*, Vol. 6, 25601, 2016.
19. Bi, Y. G., et al., "Ultrathin metal films as the transparent electrode in ITO-free organic optoelectronic devices," *Advanced Optical Materials*, Vol. 7, 1800778, 2019.

20. Lu, Z. G., et al., "Transparent multi-layer graphene/polyethylene terephthalate structures with excellent microwave absorption and electromagnetic interference shielding performance," *Nanoscale*, Vol. 8, 16684–16693, 2016.
21. Gu, J. H., et al., "Multi-layer silver nanowire/polyethylene terephylene mesh structure for highly efficient transparent electromagnetic interference shielding," *Nanotechnology*, Vol. 31, 185303, 2020.
22. Zhu, X. Z., et al., "Highly efficient and stable transparent electromagnetic interference shielding films based on silver nanowires," *Nanoscale*, Vol. 12, 14589–14597, 2020.
23. Kang, S. B., et al., "Stretchable and colorless freestanding microwire arrays for transparent solar cells with flexibility," *Light: Science & Applications*, Vol. 8, 121, 2019.
24. Chen, S., et al., "Optical waveguides based on one-dimensional organic crystals," *Photonix*, Vol. 2, 2, 2021.
25. Jiang, Z. P., et al., "Ultrathin, lightweight, and freestanding metallic mesh for transparent electromagnetic interference shielding," *Optics Express*, Vol. 27, 24194–24209, 2019.
26. Phan, D. T., et al., "Optically transparent and very thin structure against Electromagnetic Pulse (EMP) using metal mesh and saltwater for shielding windows," *Scientific Reports*, Vol. 11, 2603, 2021.
27. Wang, H. Y., et al., "Double-layer interlaced nested multi-ring array metallic mesh for high-performance transparent electromagnetic interference shielding," *Optics Letters*, Vol. 42, 1620–1623, 2017.
28. Ma, L., et al., "Transparent conducting graphene hybrid films to improve Electromagnetic Interference (EMI) shielding performance of graphene," *ACS Applied Materials & Interfaces*, Vol. 9, 34221–34229, 2017.
29. Wen, B., et al., "Reduced graphene oxides: Light-weight and high-efficiency electromagnetic interference shielding at elevated temperatures," *Advanced Materials*, Vol. 26, 3484–3489, 2014.
30. Zou, X. J., et al., "Imaging based on metalenses," *Photonix*, Vol. 1, 2, 2020.
31. Han, D. D., et al., "Bioinspired graphene actuators prepared by unilateral UV irradiation of graphene oxide papers," *Advanced Functional Materials*, Vol. 25, 4548, 2015.
32. Han, D. D., et al., "Light mediated manufacture and manipulation of actuators," *Advanced Materials*, Vol. 28, 8328, 2016.
33. Wang, D., et al., "Determination of formation and ionization energies of charged defects in two-dimensional materials," *Physical Review Letters*, Vol. 114, 196801, 2015.
34. Liu, Y. Q., et al., "Bioinspired soft robots based on the moisture-responsive graphene oxide," *Advanced Science*, 2002464, 2021.
35. Zhang, N., et al., "Flexible and transparent graphene/silver-nanowires composite film for high electromagnetic interference shielding effectiveness," *Science Bulletin*, Vol. 64, 540–546, 2019.
36. Lee, M. S., et al., "High-performance, transparent, and stretchable electrodes using graphene-metal nanowire hybrid structures," *Nano Letters*, Vol. 13, 6, 2013.
37. Anis, B., et al., "Preparation of highly conductive, transparent, and flexible graphene/silver nanowires substrates using non-thermal laser photoreduction," *Optics & Laser Technology*, Vol. 103, 367–372, 2018.
38. Han, Y., et al., "High-performance hierarchical graphene/metal-mesh film for optically transparent electromagnetic interference shielding," *Carbon*, Vol. 115, 34–42, 2017.
39. Xu, S., et al., "Cross-wavelength invisibility integrated with various invisibility tactics," *Science Advances*, Vol. 6, eabb3755, 2020.
40. Dong, F. Y., et al., "Solar-energy camouflage coating with varying sheet resistance," *Nano Energy*, Vol. 77, 105095, 2020.
41. Catrysse, P. B., et al., "Nanopatterned metallic films for use as transparent conductive electrodes in optoelectronic devices," *Nano Letters*, Vol. 10, 2944–2949, 2010.
42. Jaroszewski, M., et al., *Advanced Materials for Electromagnetic Shielding*, John Wiley & Sons, Inc Press, New Jersey, 2019.

43. Chen, X. L., et al., "Printable high-aspect ratio and high-resolution Cu grid flexible transparent conductive film with figure of merit over 80 000," *Advanced Electronic Materials*, Vol. 5, 1800991, 2019.
44. Zhao, J., et al., "An optically transparent metasurface for broadband microwave antireflection," *Applied Physics Letters*, Vol. 112, 073504, 2018.
45. Qin, C. Y., et al., "Electrically controllable laser frequency combs in graphene-fiber microresonators," *Light: Science & Applications*, Vol. 9, 185, 2020.
46. Chen, W., et al., "Flexible, transparent, and conductive $\text{Ti}_3\text{C}_2\text{Tx}$ MXene-silver nanowire films with smart acoustic sensitivity for high-performance electromagnetic interference shielding," *ACS Nano*, Vol. 14, 16643–16653, 2020.
47. Li, C. J., et al., "Highly efficient and reliable transparent electromagnetic interference shielding film," *ACS Applied Materials & Interfaces*, Vol. 10, 11941–11949, 2018.
48. Cheng, M. J., et al., "High-performance and reliable silver nanotube networks for efficient and large-scale transparent electromagnetic interference shielding," *ACS Applied Materials & Interfaces*, Vol. 13, 15525–15535, 2021.
49. Zhu, X., et al., "Highly efficient and stable transparent electromagnetic interference shielding films based on silver nanowires," *Nanoscale*, Vol. 12, 14589–14597, 2020.
50. Jiang, C., et al., "Shear modulus property characterization of nanorods," *Nano Letters*, Vol. 13, 111–115, 2013.
51. Han, Y., et al., "Crackle template based metallic mesh with highly homogeneous light transmission for high-performance transparent EMI shielding," *Scientific Reports*, Vol. 6, 25601, 2016.